Full Length Article

Heat accumulation during femtosecond laser treatment at high repetition rate – A morphological, chemical and crystallographic characterization of self-organized structures on Ti6Al4V

Georg Schnell [a],[*], Henrik Lund [b], Stephan Bartling [b], Christian Polley [a], Abdullah Riaz [a], Volkmar Senz [c], Armin Springer [d],[e], Hermann Seitz [a],[e]

[a] *Microfluidics, Faculty of Mechanical Engineering and Marine Technology, University of Rostock, Justus-von-Liebig Weg 6, 18059 Rostock, Germany*
[b] *Leibniz Institute for Catalysis, Albert-Einstein-Straße 29a, 18059 Rostock, Germany*
[c] *Institute for Biomedical Engineering, Rostock University Medical Center, F.-Barnewitz-Str. 4, 18119 Rostock, Germany*
[d] *Medical Biology and Electron Microscopy Centre, Rostock University Medical Center, Strempelstr. 14, 18057 Rostock, Germany*
[e] *Department Life, Light & Matter, University of Rostock, Albert-Einstein-Str. 25, 18059 Rostock, Germany*

ARTICLE INFO

ABSTRACT

This study presents a detailed characterization of self-organized nano- and microstructures on Ti6Al4V evoked by different scanning strategies and fluences with a 300 fs laser operating at a laser wavelength of 1030 nm. The resulting surface morphology was visualized via field emission scanning electron microscopy (FEG-SEM) images of the surface and cross-sections. X-ray diffraction (XRD)-analysis was performed to analyse changes in crystal structures. The chemical surface composition of the near-surface layer was determined by X-ray photoelectron spectroscopy (XPS). Results show a significant influence of heat accumulation while processing with high laser repetition rates on the formation, crystallinity and chemical composition of self-organized structures depending on the scanning strategy. The ablation with different laser scanning strategies led to varying dynamics of growth-mechanisms of self-organized structures, formation of intermetallic phases (Ti_3Al), sub-oxides and oxides (Ti_6O, TiO) as well as ions (Ti^{3+}, Ti^{4+}) in surface layer reliant on applied fluence. Furthermore, investigations revealed a heat-affected zone up to several micrometers in non-ablated material.

1. Introduction

Titanium alloys have a long history in various fields of application such as aerospace and automotive industry or medicine due to their excellent mechanical properties. The mechanical properties have not only led to titanium becoming established in many of these fields. Its surface properties and bioinertness, which are created by encapsulating the metallic core with a passivating oxide layer, have also played a key role [1]. However, from a technical perspective, titanium's surface partially reveals weak attributes such as low hardness, high friction coefficient and poor wear resistance [2]. From a biological perspective, smooth titanium offers only inadequate cell growth, which initially

limits the use of titanium as an implant material [3]. Therefore, numerous processes have been applied in recent decades to overcome these mentioned issues and make the alloy's surface more resistant to external stresses or provide the surface with unique features. It transpires that surface processing with short and ultrashort laser pulses has a special significance. The process allows the fabrication of a diversity of surface structures with extraordinary physical, chemical and biological properties [4–6].

Although the processing of materials with pulsed lasers present a unique opportunity to customise the surface, adverse morphology, crystallinity or chemical effects of the LT on the non-ablated material have to be considered. Heat accumulation in the non-ablated material is

---

Abbreviations: LT, laser treatment; HAZ, heat-affected-zone; PVA, preferential valley ablation; VLS, vapour-liquid-solid growth; ASG, above surface growth; BSG, below surface growth; SOT, surface offset temperature.

* Corresponding author.

E-mail addresses: georg.schnell@uni-rostock.de (G. Schnell), henrik.lund@catalysis.de (H. Lund), stephan.bartling@catalysis.de (S. Bartling), christian.polley@uni-rostock.de (C. Polley), abdullah.riaz@uni-rostock.de (A. Riaz), volkmar.senz@uni-rostock.de (V. Senz), armin.springer@med.uni-rostock.de (A. Springer), hermann.seitz@uni-rostock.de (H. Seitz).

of particular significance in this context. It accelerates chemical reactions, causes phase transformations or can lead to the formation of microcracks. The non-ablated area with altered material properties after LT is referred to as the heat-affected zone (HAZ). The HAZ is of critical relevance for the structural-mechanical performance of a component impacting crack initiation and propagation and the influence on the fatigue strength of the component [7]. The dimension and properties of the HAZ and thermal effects, such as melt formation, strongly depend on the lattice temperature of the material, which determine the material's thermo-physical response. The duration of the applied laser pulses and the physical principle of electron diffusion out of the irradiated spot and electron–phonon coupling, which are in the range of tens to several tens of picoseconds, play an essential role during LT. These interactions are schematically illustrated in Fig. 1. In the case of ablation with nanosecond laser pulses, the electrons and the irradiated solid's lattice system can be defined as a thermal equilibrium and heat transfer can occur due to electron–phonon relaxation. Thus, the HAZ dimension or laser ablation depth can be mathematically quantified by the heat diffusion length [8]. Both experimental and theoretical investigations reveal that the HAZ dimensions at ns laser irradiation can have a range from a few micrometers up to tens of micrometers [9,10]. It was shown that on Ti6Al4V surfaces, ns laser irradiation can lead to refined grains of α-Ti (size of 0.3–3 μm) with the presence of β-Ti particles next to small fragments of rutile, anatase and titanium(III) oxide (Ti_2O_3) [11]. In contrast, a transfer of heat between the electron and lattice system can, in principle, be avoided mainly by the fast interaction time of light and matter with ultra-short pulsed LT. Therefore, the electron-lattice-system's thermal behavior during the interaction with ultra-short laser pulses is described by the two-temperature model. Thus, it is assumed that sub-pico or fs pulse durations lead to lower heat input in the non-ablated material and the process is sometimes referred to as "cold ablation". Numerical studies show that the thickness of the HAZ is approximately in the nm range for fs-LT on aluminum [13]. Moreover, experimental studies have reported that a HAZ is not observable or are very small (up to a few hundreds of nanometers) in the case of ultrashort pulse laser treatment of Al [9] and TiNi [14] due to the limited thermal diffusion in the non-ablated material. But a change in grain structure Ti6Al4V due to fs-laser treatment at a fluence of 0.35 J/cm² has already been shown by Kolobov et al. [15]. Next to the initial structure, the authors obtained a nano grained sublayer of 1 μm thickness on the surface with a grain size of 80 ± 9 nm due to ultrafast cooling after LT. However, in the literature, there are also more indications of a pronounced HAZ on other metals after fs LT. For the drilling of holes in

copper, a plastic strain within the grain structure in the range of 5 μm around the drilled hole has already been observed and referred to thermal expansion and mechanical shock after LT [16]. A pronounced HAZ was reported on Cu [17] (up to 3.5 μm) and Al [10] (up to 1.5 μm) at higher fluences than the ablation threshold. Therefore, assumptions of no or small dimensions of the HAZ seem to be valid for laser-inscribed structures with an appropriate setting of the laser parameters and low repetition rates.

However, to produce the whole diversity of self-organized nano- and microstructures, an increase of the laser energy input on the surface is unavoidable since self-organized microstructures can only be realized at a certain level of fluence or number of laser shots. Fig. 2 shows the
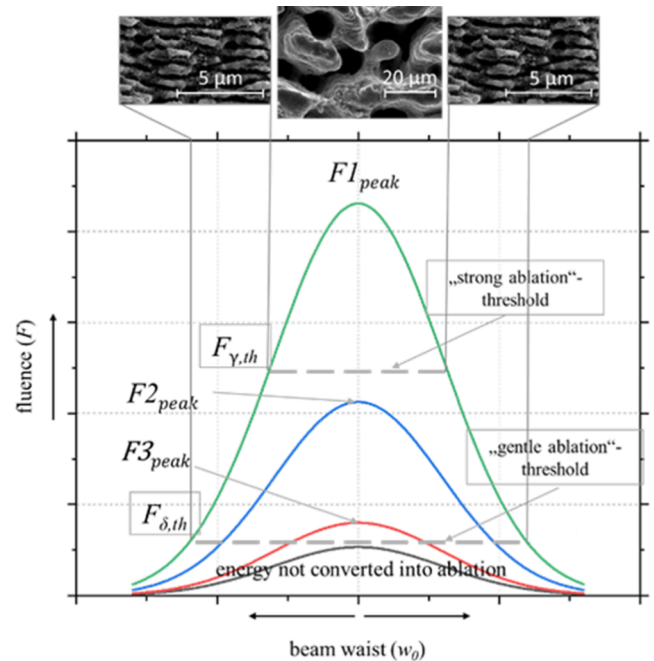
Fig. 2. Laser beam energy profile with Gaussian intensity distribution and associated formation of self-organized structures at stationary conditions. FEG-SEM-images serve as an exemplary for the uniform formation of self-organized structures at stationary laser irradiation. Graphical illustration according to [23].
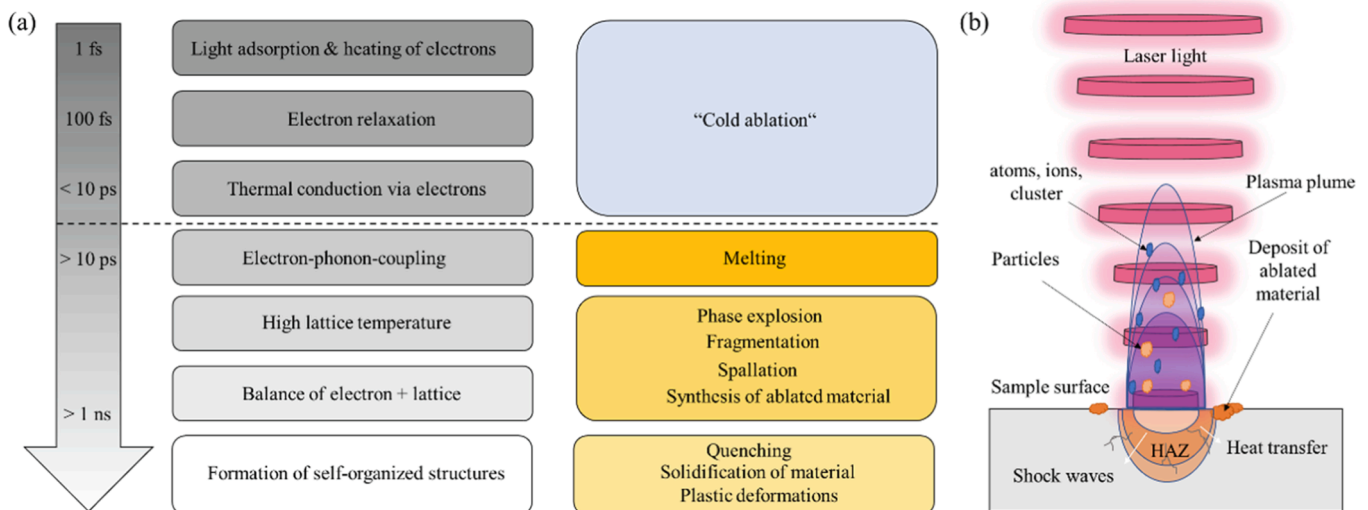
Fig. 1. Schematic illustration of the interaction principle between pulsed laser light and matter, energy transfer and associated physical phenomena and (a) ablation process and optical interaction of the laser light with the plasma plume at high repetition rates (b). Graphical illustration according to [18,19].

formation of self-organized nano- and microstructures depending on the fluence under stationary laser irradiation in a spot, sufficient laser shots and similar conditions. Essentially, LIPSS (laser-induced periodic surface structures) and microstructures can be realized via pulsed LT. These can be further divided into many difference forms (e.g. cones, spikes, pillars, grooves, microcrater) [20]. LIPSS are typically formed at fluences slightly over the ablation threshold $F_{\delta,th}$ of the material ("gentle ablation"-regime). This is the case when processing with low peak fluences (referred to as $F3_{peak}$ in Fig. 2). Moreover, in the border area with high peak fluences (referred to as $F1_{peak}$ in Fig. 2), LIPSS can be formed due to the gradual gaussian laser intensity distribution. Self-organized microstructures are typically formed in the center of the laser spot at high fluences. The abrupt increase in the ablation rate is described as the "strong ablation" threshold over a critical fluence of $F_{\gamma,th}$. The change of the ablation regime is explained by the non-linear heating of the electrons in the conduction band and subsequent electron–phonon coupling [21]. The formation of self-organized structures on titanium depending on the number of laser shots is discussed by Oliveira et al. [22]. Besides the number of laser shots, the formation also depends on several more parameters that demonstrate the complexity of these phenomena, such as the laser wavelength λ, the pulse duration t_P, the material-specific absorption coefficient α and ambient process gases. Therefore, extensive scientific effort has been made to understand the formation of self-organized structures to make these structures usable for technical applications.

For instance, LIPSS are deeply investigated, but physical fundamentals underlying this phenomenon are inconclusively clarified. The formation, the dimensions and the partly morphological and the chemical structure of LIPSS are discussed in different articles and reviews [24,25]. Nevertheless, there is an agreement that LIPSS arise from electromagnetic interactions between material and laser light [20]. These interactions affect the chemical and crystallographic properties of the surface, but this is likely to only have a minor effect on the overall performance of such a structured component. However, the altered surface properties inherent in the LIPSS can be exploited for a variety of surface functionalizations [27]. Currently, little is reported about the properties of self-organized microstructures and the formation of these structures is also under debate. Important insights have been given by Zuhlke et al. [28], who generally classified the formation of microstructures into BSG (below surface growth) and ASG (above surface growth) mounds. It is assumed that preferential valley ablation (PVA) is the primary mechanism that leads to BSG and the redeposition of ablated material and fluid flow for ASG. Even so, it is particularly striking that studies with non-stationary laser irradiation are still rare. However, non-stationary experiments and an effective scanning strategy are increasingly important in developing even faster-scanning systems, high laser pulse repetition rates, and the desire to transfer small-scale laboratory experiments to large areas. Existing literature with non-stationary irradiation mainly focuses on the number of the total over scans [29,30]. In our previous study, it was shown that, in addition to the number of over scans, the scanning pulse and line overlap significantly determine the topographical and morphological appearance of self-organized nano- and microstructures [31]. It seemed that heat accumulation is a major factor at high pulse repetition rates when discussing the formation of self-organized structures. Yet, fundamental research on this topic is rare. The dimensions of the HAZs and the characteristics of self-organized structures depending on the laser scanning strategy and fluence remain unevaluated in literature, especially on the extensively used titanium alloy Ti6Al4V.

The purpose of this study is to evaluate the effect of different laser scanning strategies on self-organizing structures on the titanium surface. In particular, the subject of the investigation is the impact of the applied scan strategy on the formation of a characteristic morphology and microstructure. The changes in the HAZ were investigated on the basis of cross-sections and conclusions were drawn about possible thermal effects in relation to the applied scan strategy. The microstructure was

analyzed in detail on the basis of cross-sections using field-emission gun scanning electron microscopy (FEG-SEM), X-ray diffraction (XRD), X-ray photoelectron spectroscopy (XPS). Consequently, guidelines for fs-LT with high repetition rates are given, which can be used for tailoring the morphology, crystallinity and chemical composition of the surface.

2. Materials and methods

2.1. Sample preparation and fs-laser treatment

Ti6Al4V plates (10 × 10 × 4) mm, S + D Spezialstahl Handelsgesellschaft GmbH (Stelle, Germany) were mechanically polished with silicon carbide abrasive sandpaper from P320 (t_1 = 4 min) to P600 (t_2 = 4 min) and afterwards with P1200 (t_3 = 8 min) to ensure homogeneity and low roughness of the initial surface (Sa = (0.03 ± 0.01) μm).

A commercial Yb-doped fiber laser of the type of UFFL (Active Fiber Systems GmbH, Jena, Germany) with a pulse duration of 300 fs was used to irradiate the polished Ti6Al4V surfaces. The settings for the fluence are listed in Table 1. The pulse energy required to calculate the fluence was determined from the average power of the laser, which was measured using a power meter of the type F150A-BB-Sh-26 (Ophir Optronics, Israel, Jerusalem). The repetition rate f_{REP} was set to 226.8 kHz. For this research, linear polarized light with a wavelength of 1030 nm was applied. The laser system is integrated into a five-axis micromachining center of the type Microgantry GU4 (Kugler GmbH, Salem, Germany). Each structure pattern was produced four times on a squared shaped area of 7 × 7 mm under similar laser-irradiation conditions for the subsequently performed analysis.

Two fundamentally different scanning strategies ($S1$ and $S2$) were used to assess the impact of those on the surface features. The processing was based on the results of a previous study. A high scanning pulse overlap (PO) and a high line overlap (LO) have found to be particularly interesting for obtaining a high roughness modification or a homogeneous distribution of nanostructures, respectively [31]. The PO was controlled by varying the scanning speed v_{Si}. The LO was set by the scanning line feed Δd as schematically illustrated in Fig. 3. The calculation for the PO and LO are based on Eqs. (1) and (2), respectively:

$$PO = \left(1 - \frac{v_{Si}}{d_f \times f_{REP}}\right) \times 100\% \qquad (1)$$

$$LO = \left(1 - \frac{\Delta d_{Si}}{d_f}\right) \times 100\% \qquad (2)$$

where d_f is the circular focus diameter, f_{REP} is the repetition rate and Δd is the space in scanning line feed [32].

For scanning strategy $S1$, PO was 90 % (v_{S1} = 0.81 m/s) and LO was set to 50 % (Δd_{S1} = 18 μm). Similarly, for scanning strategy $S2$, PO (v_{S2} = 4.08 m/s) was 50 % and LO (Δd_{S1} = 4 μm) was set to 90 %. For both strategies, the number of over scans was 50. Thus, the energy input on the surface by laser irradiation is on a comparative level. The beam was positioned via two galvanometric mirrors integrated in a scan head of the type intelliSCAN 14 (Scanlab GmbH, Puchheim, Germany) and focused by an F-theta lens with a focal length of 163 mm, leading to a circular focus diameter of d_f = 36 μm at $1/e^2$ intensity (Gaussian laser beam profile). The spot diameter was used for all laser parameter calculations.

After LT, cross-sections were made from the structured samples to provide detailed information about the structure formation and

Table 1
Variation for the laser fluence valid for both *S1* and *S2*.

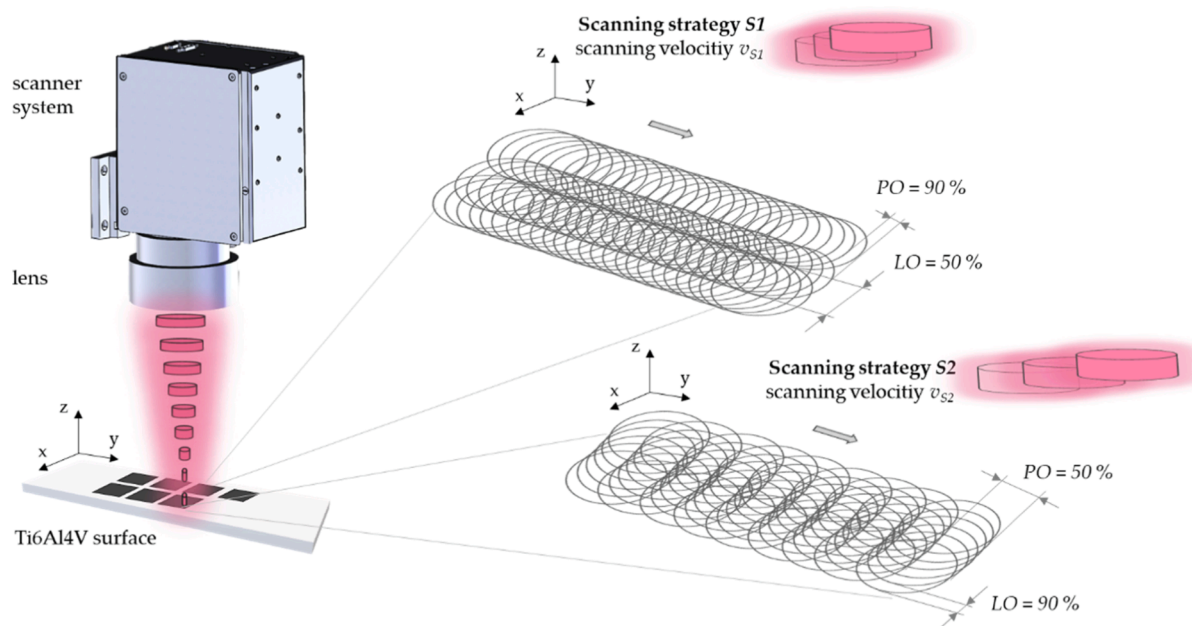| Pulse energy [μJ]	1.41	4.98	8.77	28.66	48.50
Fluence [J/cm²]	0.14	0.49	0.86	2.81	4.76

Fig. 3. Schematic illustration for laser scanning strategies *S1* and *S2*. Graphical illustration according to [31].

dimensions of the HAZ for different scanning strategies and fluences. Therefore, specimens were face embedded in EpoxiCure™2 Epoxy Resin and EpoxiCure™2 Epoxy Hardener (Buehler, ITW Test & Measurement GmbH, Esslingen, Germany) and finished with Tegra-Pol 15 grinding and polishing device (Struers GmbH, Willich, Germany) in the following steps: (1) Grinding with 1200, 2000 and 4000 grit sandpaper, (2) polishing with Diamond Suspension 3 μm and 1 μm, (3) polishing with Fumed Silica Suspension 0.2 μm waterfree (Cloeren Technology GmbH, Wegberg, Germany), (4) polishing cloth of the type Chemomet Polishing cloth (Buehler ITW Test & Measurement GmbH, Esslingen, Germany). Etching was subsequently carried out with ammonium bifluoride and then cleaned with distilled water and ethanol.

2.2. Characterization and analysis

2.2.1. FEG-SEM-Imaging

The top-imaging and cross-section-imaging of the laser-treated samples were performed via field-emission gun scanning electron microscope (FEG-SEM (abbreviated below as SEM)) of the type Merlin VP compact (Carl Zeiss AG, Oberkochen, Germany). ImageJ software (Version 1.52, available as freeware online from https://imagej.nih.gov/ij/) was used to characterize the dimension of the microstructures and HAZs.

2.2.2. XRD-Analysis

XRD patterns were recorded either on a Panalytical Empyrean θ/2θ-diffractometer (PANalytical GmbH, Almelo, Netherlands) equipped with a PIXcel 3D detector system or a Panalytical X'Pert θ/2θ-diffractometer equipped with Xcelerator detector both using automatic divergence slits and Cu kα1/α2 radiation (40 kV, 40 mA; λ = 0.15406 nm, 0.154443 nm). Cu beta-radiation was excluded by using nickel filter foil. Data collection was done with a velocity of $0.011°s^{-1}$ (XPert) or $0.017°s^{-1}$ (Empyrean), respectively. The reference and the laser-structured samples (small plates) were mounted on modelling clay and fixed at the correct specimen height within the sample holder. The intensities obtained as a result of the incidence of the X-Ray beam on the surface of the sample were converted from automatic to fixed divergence slits (0.25°) for further analysis. Peak positions and profile were fitted with Pseudo-Voigt function using the HighScore Plus software package (Panalytical). Phase identification was done by using the PDF-2 database 2016 of the

International Center of Diffraction Data (ICDD).

2.2.3. XPS-Analysis

The XPS (X-ray Photoelectron Spectroscopy) measurements were performed on an ESCALAB 220iXL (Thermo Fisher Scientific, Waltham, MA, USA) with monochromated Al Kα radiation (E = 1486.6 eV). Samples were prepared on a stainless-steel holder with conductive double-sided adhesive carbon tape. The electron binding energies were obtained with charge compensation using a flood electron source when necessary and referenced to the C 1 s core level of adventitious carbon at 284.8 eV (C–C and C–H bonds). For quantitative analysis, the peaks were deconvoluted with Gaussian-Lorentzian curves using the software Unifit 2021 (Unifit Scientific Software GmbH, Leipzig, Germany, 2020). The peak areas were normalized by the transmission function of the spectrometer and the element-specific sensitivity factor of Scofield.

3. Results & discussion

3.1. SEM of cross-sections and top surfaces

All laser parameter settings resulted in successful modification of the surface, as summarized in Fig. 4 for both scanning strategies. Detailed SEM-images (appendix A.1-A.5) reveal the formation of LIPSS, micrometric ripples (MR, also designated as micron-spaced grooves), microcraters (also designated as domes) and cones on the irradiated surfaces, which also occur in hybrid patterns leading to a dual-scale roughness. A comparison of the surfaces obtained with both scanning strategies at equal levels of applied fluences reveals clear differences in the extent and dimension of the self-organized structures. The SEM-images revealed that a high scanning *PO* (identical to strategy *S1*) resulted in a pronounced waviness evoked by trenches, whereas an equivalent level of scanning line overlap (similar to strategy *S2*) leads to a homogeneous distribution of nanostructures at low fluences. The formation of microstructures starts at a lower level of fluences with *S1* compared to *S2* (see Fig. 4). These results are in line with our comprehensive study on various settings of *PO* and *LO* [31].

We assumed that the reason for the formation of self-organized microstructures at a lower level of *PO* compared to a high level of *LO* with a comparable fluence is the occurrence of heat accumulation at high repetition rates and the resulting different temporal and geometric
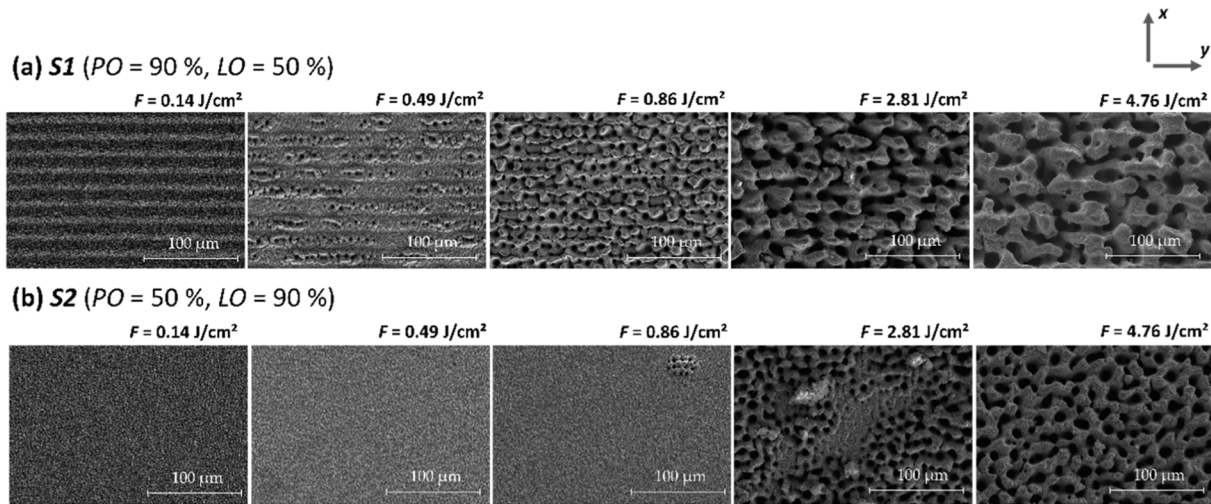
Fig. 4. SEM-Images of structured surfaces with *S1* (a) and *S2* (b) at increasing laser fluence.

distribution of heat on the surface. First, the hypothesis is in agreement with the findings of other groups that pointed out that heat accumulation is an essential part of the ablation process when realizing laser-inscribed structures at stationary conditions with similar, high repetition rates as used in this study. Heat accumulation was considered to be a significant phenomenon for drilling micro holes from specific energy input with increasing repetition rates [33]. The authors explain that residual heat remains when the energy absorbed exceeds the energy required for the ablation of the material, which is always the case when processing with ultrashort laser pulses. If only evaporation is considered as the removal mechanism of the material, the amount of heat remaining in the non-ablated material, according to Weber et al. [33], can be calculated as follows:

$$Q_{heat} = \eta_{Abs} x E_{Pulse} - V_{Evap} x h_{Evap} - Q_{Vapor}. \tag{3}$$

Here, $\eta_{Abs} \times E_{Pulse}$ quantifies the absorbed energy, by the absorptance of the material and the applied energy on the surface. $V_{Evap} \times h_{Evap}$ represents the ablation energy, where the evaporated volume and the volume-specific enthalpy for the evaporation are considered. Q_{Vapor} specifies the energy amount by which the vapor is overheated during expansion. In addition to this assumption, it should be noted that ablation is probably also caused by other mechanisms such as thermo-mechanical fragmentation or spallation [34] or phase explosion [35]. When examining the processing with single pulses or low repetition rates, the heat input in the non-ablated material is low and the effects on the performance of the workpiece are marginal. But when considering processing with high repetition rates, the heat introduced cannot be

sufficiently dissipated and heat accumulation occurs. Heat accumulation had already been observed for laser-inscribed structures at repetition rates over 200 kHz [36] and at 250 kHz [37]. A workpiece temperature increase was demonstrated by numerical simulation at high repetition rates [33,38]. According to the findings, the melting point of the material can be exceeded and consequently the process quality is affected by undesirable melting phenomena. In sum, the effect of thermal input in the non-ablated material was demonstrated for laser-inscribed structures for stationary irradiation and represents important findings for the discussion of the formation of self-organized structures.

At low fluences ($F = 0.14$ J/cm^2), the resulting morphology of the scanning strategy *S1* and *S2* looks relatively similar (Fig. 5 (a) and (b)). Both surfaces reveal an overall cover by LIPSS and MR. The generation of LIPSS on titanium and titanium alloys has been demonstrated in numerous studies applying fluences from 0.067 J/cm^2 up to a few tenths of J/cm^2 [26,31,39,40]. As previously mentioned, the formation of LIPSS is still under discussion, but experimental results show that the appearence of LIPSS on metals can be understood as a successive process. The first applied laser pulses lead to a randomly distributed nanostructure. It is assumed that the random formation of nanostructures after a few pulses results from a differentially distributed plasmonic absorption due to nanostructural defects [18]. These nanostructures are followed by the formation of a nanoscale dynamic melt due to electron–phonon coupling and diffusion of hot electrons [41]. Subsequently, hydrodynamic effects such as spallation of cavitation bubbles and melt flow due to surface tension gradients result in nano-protrusions, nanocavities and nanorims after solidification [42]. The
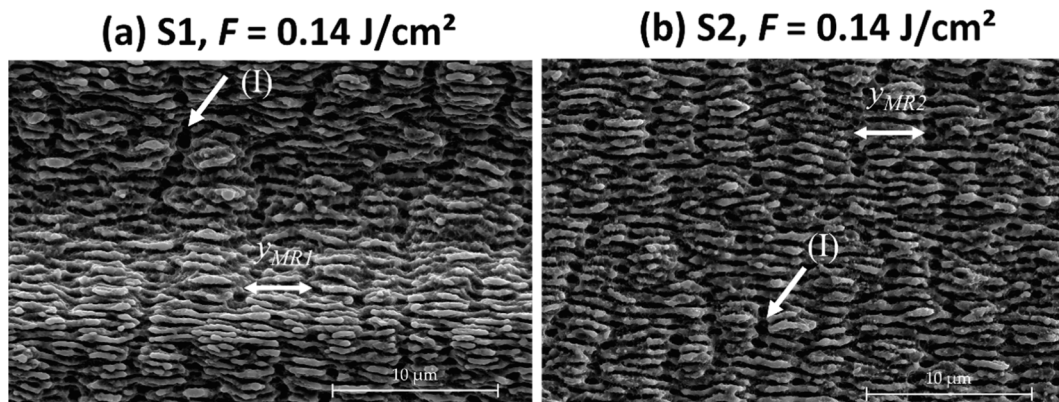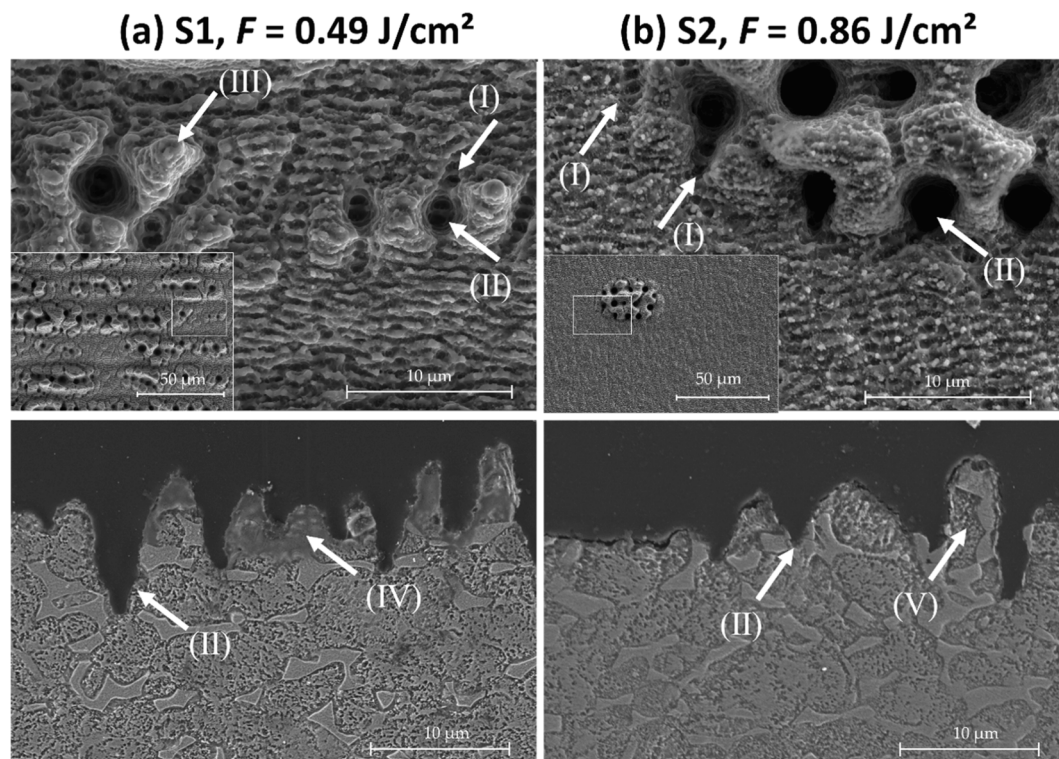

Fig. 5. Surface-SEM-Images for strategy *S1* (a) and *S2* (b) at a fluence of 0.14 J/cm^2, (I) MR, y_{MRi} indicate the determination of the spatial distances of MR.

interference between the laser light and the polarization of the surface plasmons leads to the spatial modulation of the introduced energy on the surface if enough free electrons are present due to non-linear processes in the conduction band [43]. Due to the refraction at the incident nanostructures, the incident light is coupled, and surface plasmons are polarized in the subsequent laser pulses [44]. As a result, a spatially modulated heating of the surface after the laser pulse interaction with the surface and the formation of periodic structures is evoked. Resonant coupling of the laser light with the polarized surface plasmons occurs from a certain degree of surface modification, which leads to a much more effective build-up of nanostructures. The clear delineation of fused periodic regions can be characterized as low spatial LIPSS, which are typically orientated perpendicular to the polarization and clearly visible for scanning strategy *S1* and *S2* at a fluence of 0.14 J/cm^2 [45]. Detailed insights into this phenomenon are given in the literature [18,28]. MR (Fig. 5 (a)+(b)-(I)) are orientated parallel to the polarization of the laser light with a typically spatial periodicity of 2.5–5 μm [31,47,48]. Therefore, the measured distances between the MR with $y_{MR1} = 3.4 \pm 0.7$ μm for *S1* and $y_{MR2} = 3.3 \pm 0.7$ μm for *S2* at $F = 0.14$ J/cm^2 are in good agreement with previous studies. The formation of MR is not yet fully understood, but is associated with electromagnetic scattering due to interferences of excitation of surface plasmon waves with the incident laser light, heat transfer and hydrodynamic effects during laser treatment [47–49]. Up to a fluence of 0.14 J/cm^2, the entire formation process of self-organized features can be summarized as phase 1 (denoted as formation of self-organized-nanostructures and MR).

When considering Fig. 6 (a) and (b), it is evident that MR (I) serve as precursor sites for the formation of larger features. At fluences of 0.49 J/cm^2 and 0.86 J/cm^2, microcraters (II) are formed where MR have been located, regardless of the scanning strategy. The growth of the microcraters is attributed to scattering effects on the walls of the precursor sites, which lead to an increasing local level of fluence and consequently to the successive expansion of the interspaces by the following laser shots. This ablation phenomenon is described as preferential valley ablation (PVA) and therefore, our observations agree with the literature

[28]. However, a closer comparison of the scanning strategies in Fig. 6 reveals that the formation of cone-like features (phase 2) differ fundamentally. At a fluence of 0.49 J/cm^2, strategy *S1* evoked a high area percentage of cone-like microstructures (Fig. 6 (a) –(III)), which are primarily located in the trenches and thus evoked by high laser intensities in the centre of the Gaussian laser beam. The cones are covered with piled-up melt, which indicates that the melting temperature of the material has been exceeded. The corresponding cross-section (Fig. 6 (a) –(IV)) reveals that the grain structure within the cones has been modified. Therefore, the underlying mechanism leading to the formation of self-organized microstructures in phase 2 appears to be predominantly characterised by the redeposition of material ablated in the valleys on the peaks of the surface for *S1*. This mechanism is designated as vapor–liquid-solid (VLS) growth and had already been shown for ablation with nanosecond pulsed laser [50], whereby heat accumulation basically occurs. VLS describes the interaction of the plasma plume and particles, which is caused by PVA, with the molten tops and results in a successive build-up of self-organized structures. This mechanism is critical to the applied fluence [28]. With strategy *S2* at a fluence of 0.86 J/cm^2, island-like microscale clusters are formed randomly on the surface (Fig. 6 (b)), which are probably evoked by material inhomogeneities, resulting in different local ablation. The growth seems to be based on the PVA principle. Even at this much higher applied fluence compared to strategy *S1*, only nanoscale melts can be observed on the surface. This observation suggests a subordinate role of the melt in the formation of the cones by strategy *S2*. In contrast to *S1*, the grain structure within the cones has not changed noticeably with *S2* (Fig. 6 (b) – (V)), which emphasizes the assumption of PVA of growth for microstructures at $F = 0.86$ J/cm^2. The build-up of the microcrater progresses until cones are formed, which can be seen in Figure A4 (*S2*) and corresponds with findings in the literature [25]. Self-organized microstructures (columns, spikes, cones) were also observed on titanium and its alloys at fluences ranging from 0.35 to 47 J/cm^2 [29,31,39,51].

It can be concluded that heat accumulation by Q_{heat} plays an important role in the formation of self-organized features, at least at a
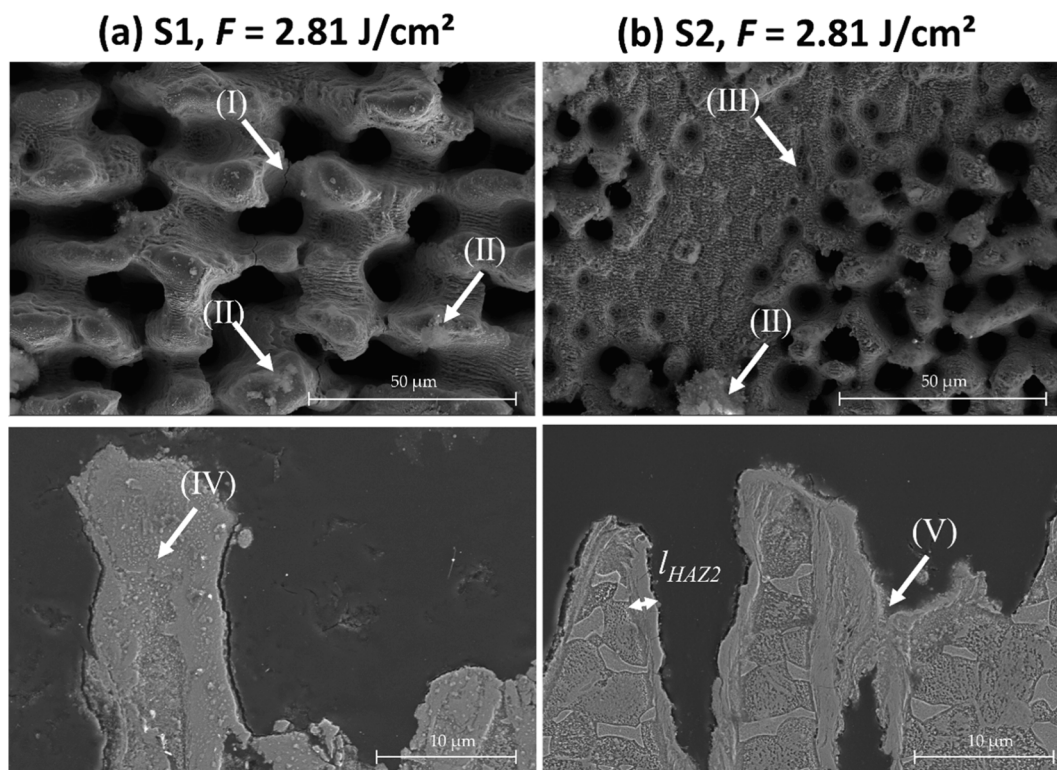

Fig. 6. SEM-Images of surfaces and cross-sections for strategy *S1* at a fluence of 0.49 J/cm^2 (a) and *S2* (b) at a fluence of 0.86 J/cm^2. (I) MR serve as precursor sites for (II) microcrater and (III) cone-like microstructures with modified (IV) and original grain structure (V) depending on the scanning strategy.

fluence of 0.49 J/cm^2 while processing with *S1*. For strategy *S1*, which is based on a high pulse overlap, it can also be inferred that the surface does not significantly cool down as it probably does for strategy *S2*. The local interaction time is considerably greater on the same irradiated area with strategy *S1* than with strategy *S2* due to the geometric distribution of consecutive pulses. This local interaction time can be calculated according to $t_{int} = d_f/v_{Si}$. For *S1* the interaction time amounts to $t_{intS1} = 44.1$ µs and for *S2* to $t_{intS2} = 8.8$ µs. This difference leads to a different distribution of Q_{heat} on the surface for *S1* compared to *S2*. It can be concluded that LT with *S1* results in inefficient heat dissipation and a higher level of heat accumulation at the surface. The time delay of approximately 4.4 µs between subsequent pulses at a repetition rate of 226.8 kHz seems to evoke a surface offset temperature (SOT) due to insufficient heat dissipation by the limited thermal conductivity of the material. The SOT can result in a phase transformation to the liquid phase of the material when crossing the melting point of titanium ($T_M = 1680$ °C). These assumptions and observations are consistent with numerical simulations of the heat accumulation phenomenon on other metals [33]. The results show that the surface cannot cool down to the initial temperature when using high repetition rates since a significant surface cool down can last tens of µs. Therefore the SOT can be increased steadily from pulse to pulse. Thus, subsequent pulses reach a still heated or liquid phase, which favors hydrodynamic effects and structure formation in the sense of VLS growth for *S1*. This is even more evident when considering the formation of microstructures with strategy *S1* at a fluence of 2.81 J/cm^2 in Fig. 7. The cones are covered with melt or even consist entirely of reformed material, which can be seen in Fig. 7 (a) – (IV). It is particularly interesting that partial micro-cracks are visible with strategy *S1* (Fig. 7 (a) – (I)). For LT following strategy *S1* micro-cracks were observed starting from a fluence of 2.81 J/cm^2 (Figure A4-A5 (*S1*)).

All these phenomena can be related to a high heat exposure and suggest a high level of residual Q_{Heat}. In contrast, the growth mechanism for scanning strategy *S2* at 2.81 J/cm^2 was still dominated by PVA. Here

the material seems to be ablated rather than melted. But Fig. 7 (b)-(V) also shows signs of melting and merging of adjacent structures. However, the original grain structure in the underlying substrate is barely affected and the self-organized microstructures evince a HAZ of $l_{HAZ2} = 1.5 \pm 0.2$ µm at a fluence of 2.81 J/cm^2 for *S2*. It should be noted that structural changes resulting from heat diffusion in the non-ablated material cannot be clearly separated from already ablated and re-melted material on the surface. A merging of cones can be observed for both strategies with increasing fluence, and therefore, the total number of cones is decreasing (Fig. A3 (*S1*) to A.5 (*S1*) and A.4 (*S2*) to A.5 (*S2*)). The cones grow in diameter, and the spaces between them also increase. This is in line with other studies [28]. Moreover, a significant amount of micrometer-sized agglomerates ((Fig. 7 (a + b) –(II) and A.4-A.5)) are deposited on the structured surfaces at both strategies from fluence from 2.81 J/cm^2, which represents an additional source for the VLS growth. Similar large agglomerates could not be observed at lower fluences.

Lastly, if the fluence is increased further to 4.76 J/cm^2, the build-up of the structures by melt flow takes on a crucial role for strategy *S1*, which is evident when considering the SEM-image in Fig. 8 (a)-(I). The solidified melts on the crater walls indicate a creep up of molten material. The Marangoni convection is under discussion to evoke the flow of melt from the valleys to the peaks [48]. The effect is known to be induced by temperature gradients. In the valleys, the temperature rises due to laser irradiation and where the interfacial tension is low, leading to the creep of the melt due to the surface tension gradient. The hydrodynamic growth mechanism was also suggested for the growth of cones on silicon [53]. The high differences in temperature cause residual stresses and subsequently the formation of cracks in the solidified melt (Fig. 8 (a)-(II)). With *S2*, growth seems to still be dominated by PVA and VLS (Fig. 8 (b)-(III)). However, changes in grain structure were determined up to $l_{HAZ2} = 9$ µm. Melting phenomena were also observed applying strategy *S2*, but with significantly less pronounced and fewer cracks (Fig. 8 (b)-(IV)). For a fluence of 4.76 J/cm, it can be concluded

Fig. 7. SEM-Images of surfaces and cross-sections for strategy S1 (a) and S2 (b) at a fluence of 2.81 J/cm^2, (I) microcracks, (II) agglomerates, (III) MR, (IV) cone (V) merging of cones, l_{HAZ2} indicate the determination of the length of a HAZ for *S2*.

(a) S1, F = 4.76 J/cm² (b) S2, F = 4.76 J/cm²
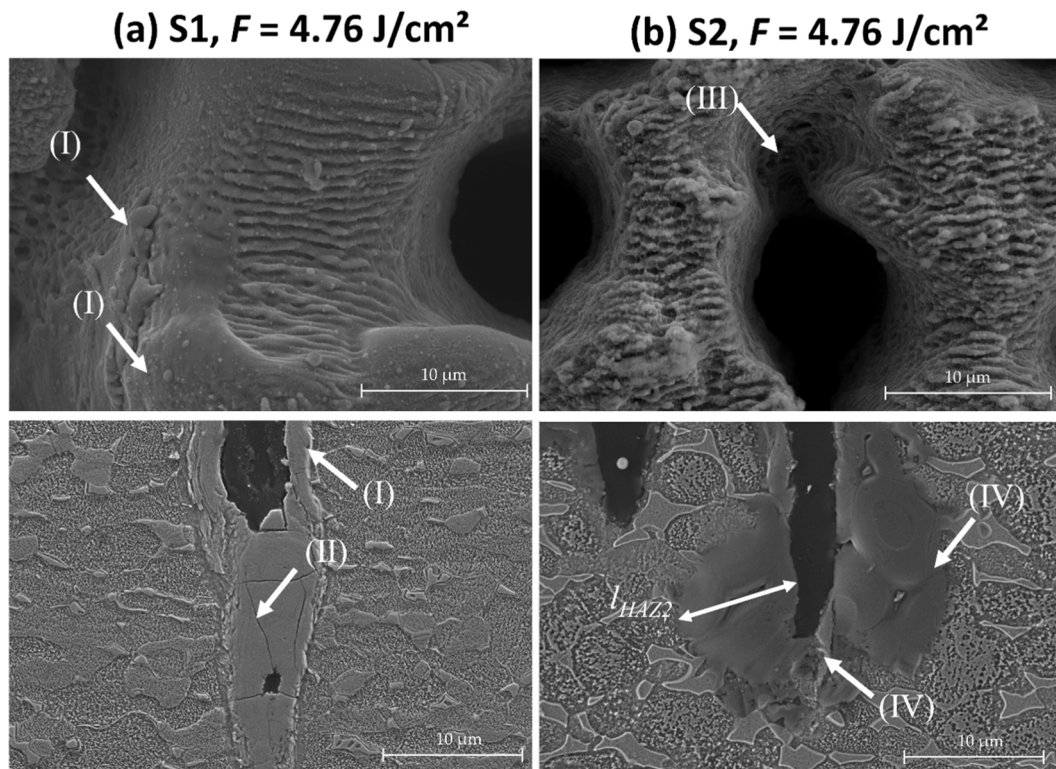
Fig. 8. SEM-Images of surfaces and cross-sections for strategy *S1* (a) and *S2* (b) at a fluence of 4.76 J/cm², (I) solidified melt flow, (II) microcracks in lagging melt, (III) micro craters, (IV) heat impact on grain structure, l_{HAZ2} indicate the determination of the maximum length of a HAZ for *S2*.

that also *S2* leads to a pronounced HAZ.

In summary, the formation of self-organized microstructures is determined by PVA, VLS and melt flow and strongly depends on the applied laser fluence and scanning strategy, as illustrated in Fig. 9. The SEM images have primarily confirmed these findings and show that a good balance is needed between the applied energy and the design of the scan strategy in order to specifically use effects such as ablation and heat accumulation for the formation of the microstructures.

3.2. XRD-analysis

First, diffraction data of an untreated specimen were recorded in Bragg-Brentano-geometry to gain peak positions, composition and unit cell data of the present phases. Two phases were found, which can be identified as hexagonal closed (Ti-hcp, α) and cubic closed (Ti-ccp, β) packed structures, exhibiting strongly preferred orientation features. However, peak positions were shifted compared to pure Ti references.
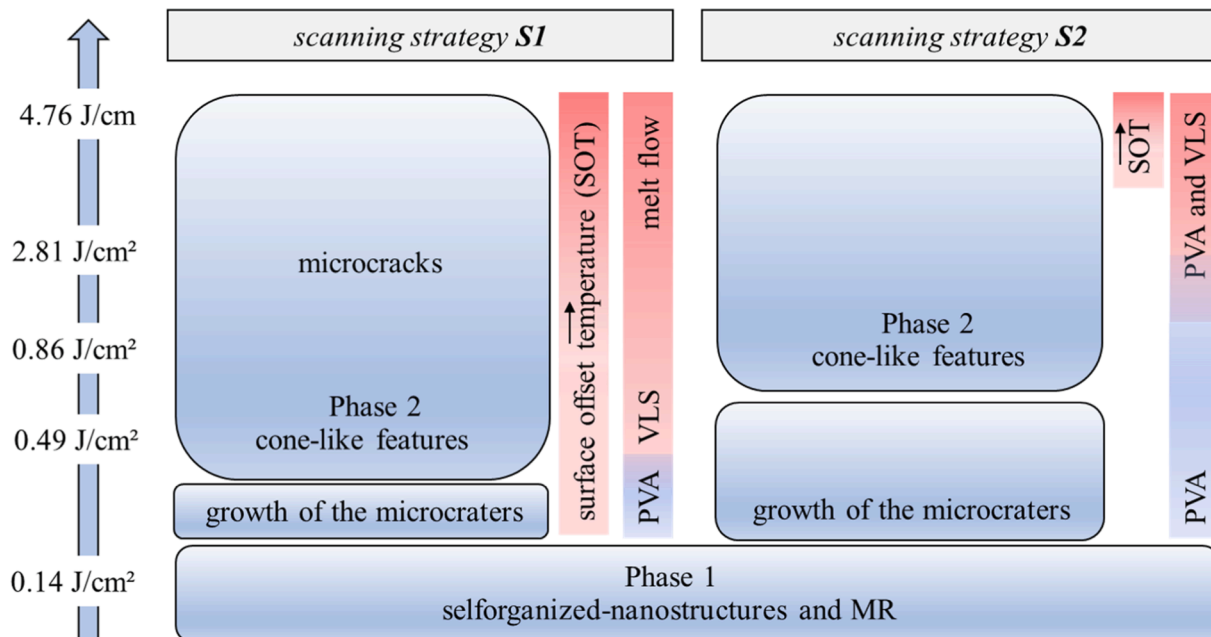
Fig. 9. Schematic illustration on the formation of self-organized structures with corresponding, dominating growth mechanism depending on scanning strategy and applied fluence.

8

Unit cell data, received by the Pawley-fitting method, were in agreement with previously published datasets and were used to further analyse LT samples by applying identical data collection strategy (Table B1).

The evaluation of different phases present after LT employing *S1* with different fluences is visualized in Fig. 10. Even at low fluences of 0.49 J/cm^2 the formation of titanium oxides (Ti$_6$O, ICDD pdf 01–073-1118) can be seen. Its content is increasing as seen by the increase of corresponding ($\overline{11}2$) Bragg peak intensity at 40.38° 2θ, if the fluence is further increased to a value of 0.86 J/cm^2. Ti is oxidized to a higher extent since TiO is identified from the diffraction data (ICDD pdf 01–089-0510) in addition as a minor phase. Formation of Ti-oxides during LT have been reported for ns-LT by Lavisse et al. [54] reasoned by diffusion of oxygen into the substrate due to melting of laser-treated near-surface regions. Further, Kolobov et al. [55] assume a deposition of oxidized particles as a mechanism for the formation of an oxide layer on the surface during fs-LT with a repetition rate of 250 kHz, which is in line with the observation of TiO$_x$ formation. Therefore, it is suggested that a strong oxygen diffusion into the alloy occurred possibly by melting of the surface layer or redeposition of ablated material in the air from a value of 0.49 J/cm^2. The finding agrees with the assumption of VLS growth revealed by SEM-Images (Fig. 6 (a)) for *S1* starting from 0.49 J/cm^2 (due to SOT > T$_M$).

Due to a shoulder at 40.68° 2θ the formation of AlTi$_3$ can be assumed, which is also present if higher fluences ($\geq$2.81 J/cm^2) are applied. Intermetallic compounds are commonly observed in the melt zone of laser joined materials [56]. Its formation may be caused by the reduction of Ti content in the alloy due to ongoing oxidation to TiO$_X$ combined with LT induced melting and Al enrichment. As mentioned later, Al content in the first few nm-range of the surface decreased with an increasing level of fluence (see XPS data in Fig. 12) and a prerequisite for the genesis of pronounced Ti$_3$Al phases is a sufficiently high content of Al [1]. At 2.87 J/cm^2 the formation of TiO is visible more clearly by the presence of intense main reflection peaks at 37.24 (1 1 1), 43.19 (2 0 0) and 62.67° (2 2 0), respectively (ICDD pdf 01–072-2741). In addition, the intensity of Bragg peaks with regard to Ti$_6$O are much more intense, emphasizing a higher extent of oxidation during LT with increased fluences. Other Ti oxides, i. e. Ti$_6$O, Ti$_3$O, Ti$_2$O or even TiO$_2$ [57], were not observed unequivocally due to similar hexagonal unit cell dimension, diffraction peak width and overlapping but these cannot be ruled out as minor phases. In addition, other oxides formed from the alloy (Al$_2$O$_3$, VO$_X$) were not observed, mainly because of the low content of Al and V. An effect of surface roughnes on data quality was not observed because data collection in grazing incidence mode have not been performed in this study.

Quantitative evidence can be derived by analysis of diffraction data by the RIR method [58], which was chosen due to several uncertainties as mentioned above. However, the trends describe the process outlined before sufficiently, especially the increased formation of Ti oxides if higher fluences are applied (Fig. 11 (a)).

If *S2* is applied for LT the formation of Ti oxides is firstly observed at a fluence of 2.81 J/cm^2 (Fig. 11 (b) and Figure B1), which is in line with the assumption of dominating PVA growth of microstructures for *S2* up to that level of fluence. In addition, a AlTi$_3$ phase is present from a fluence of 2.81 /cm^2 with *S2*. To summarize, findings from the XRD data confirm the assumptions of different dynamics of the formation of self-organized microstructures driven by heat accumulation.

3.3. XPS-analysis

XPS investigations were carried out to qualitatively and quantitatively describe the chemical changes of the surfaces and the near-surface regions caused by LT and heat accumulation. Serious chemical changes have a direct influence on the physical properties of the surface and can thus change the performance as an implant material or high-performance construction material. For example, chemical changes contribute to biocompatibility and associated changes in surface energy affect cell reactions and wetting properties [40,51,59]. Since only the electrons generated in the first nm of the surface escape and can be detected, XPS is chosen to analyse changes in surface chemistry of samples after LT with *S1* and *S2*.

The XPS-survey spectra for the reference and LT samples with both strategies *S1* and *S2* (Figure C1 (a,d,g,j)) show O, C, Ti, Al and minor amounts of V and N as the most abundant elements at the surface. Also, negligible amounts of F can be detected, which could be a result of sample handling and/or mounting. The corresponding concentrations of O, C, Ti, Al, V and N are shown in Table 2 and Table C1 for all samples. The detected amount of Al is separately depicted in Fig. 12. At low fluences, the Al concentration on the surface is increased compared to the reference due to an enrichment of Al^{3+} after LT for both *S1* and *S2* [40]. With increasing fluence, a decrease of the Al concentration is observed. Interestingly for the two highest fluence values for *S2*, the Al concentration drops below the reference sample. The Ti content is reduced after LT for all samples, but changes depending on the fluence are not visible (see Table C1). The different portions of Al and Ti elements on the surface depending on the fluence, can be explained by a significant higher ablation threshold of Al compared to Ti [60], which results in different ablation dynamics during LT. Furthermore, all laser-treated surfaces exhibit a higher concentration of C compared to the reference (Table 2), which is attributed to the adsorption of hydrocarbons over a period of time in the ambient air. Detailed insights into the adsorption of hydrocarbons on laser structured surfaces and correlations to surface wettability are reported in the literature [40]. A relevant amount of N can be observed in the XPS spectra, which is well described for Ti and its affinity for attracting O and N [1]. However, no significant alteration in O or N could be observed after LT.

More insights into the chemical composition of the near-surface layer are presented in corresponding high-resolution spectra of Ti 2p, Al 2p, C 1 s and O 1 s regions (see Figure C1 and C2). Due to exposure to air, oxidation of the surface on all samples is evident by the appearance of peaks at 530.1 eV and 531.2 eV in O 1 s (see representative Figure C2d) related to TiO$_2$ and Al$_2$O$_3$ [62], respectively. Contrary to XRD, the formation of Al$_2$O$_3$ is confirmed by a peak at 74.0 eV in Al 2p spectra (Figure C1) [63]. The observed native oxide layer with a thickness of several nm on the reference is in line with the literature [65]. Up to $F =$ 0.49 J/cm^2, a peak at 71.2 eV in Al 2p spectra can be found, suggesting the presence of metallic Al. For Ti, the corresponding metal peak at about 453.2 eV disappears at $F > 0.86$ J/cm^2. Compared with the reference sample, the thickness of the oxidic layer increases by LT and
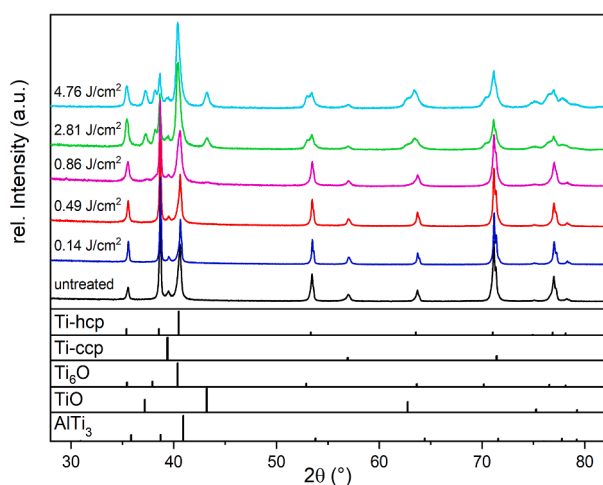

Fig. 10. X-ray diffraction pattern of LT treated Ti6Al4V using *S1* and different fluences. Reference diffraction peak positions are given according to ICDD pdf reference cards. Ti$_6$O (01–073-1118), TiO (01–072-2741) and AlTi$_3$ (01–072-5005), respectively.
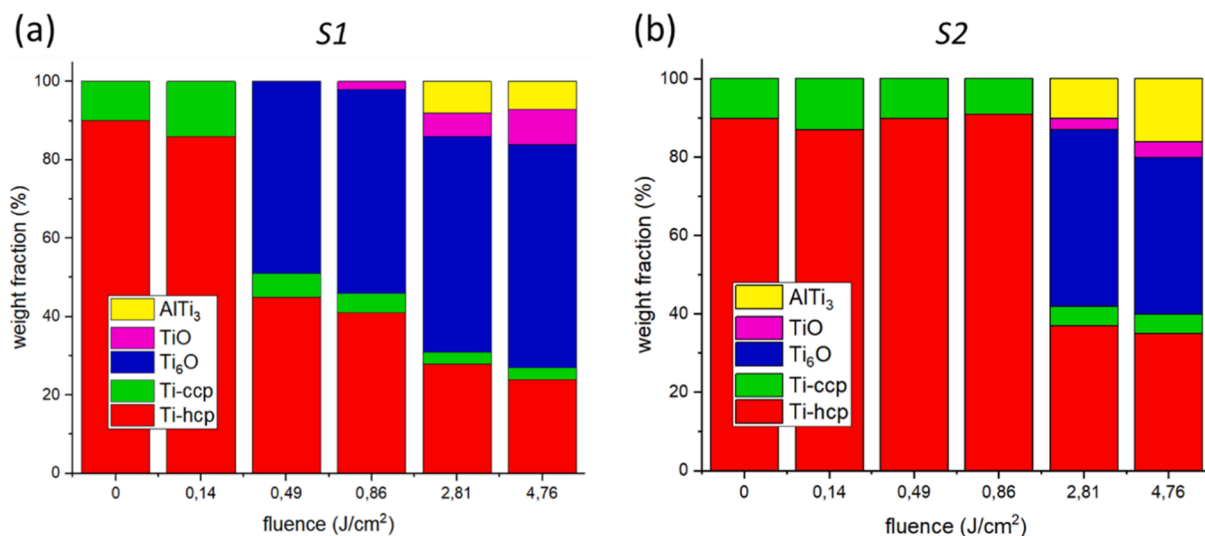
Fig. 11. Composition of Ti6Al4V after laser treatment using *S1* (a) and *S2* (b) calculated by the RIR-method.
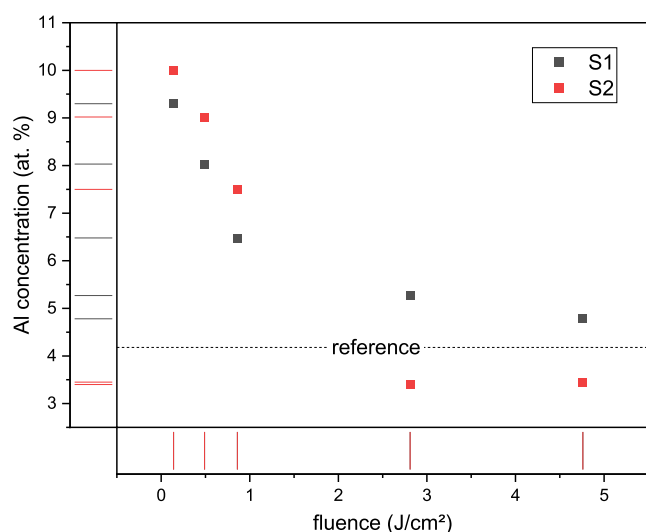

Fig. 12. Total portion of Al on the surface of reference and structured samples with *S1* and *S2* depending on the fluence.

Table 2

Chemical composition (at.%) of the samples obtained by XPS-analysis. Only main components on the surface are listed. The changes in Al-concentration are illustrated in Fig. 12.

Sample	O (at.%)	C (at.%)	Ti (at.%)	Al (at. %)	N (at.%)
Reference	50.8	25.5	18.3	4.2	0.7
S1 at 4.76 J/cm^2	48.6	28.4	16.9	4.9	0.6
S2 at 4.76 J/cm^2	46.6	33.9	14.2	3.5	0.8

grows with the applied fluence for both *S1* and *S2* (see Table C1). It should be further noted that this finding seems to be independent of the generated surface morphology. A significantly increased oxide layer thickness after LT determined by glow-discharge optical emission spectroscopy (GD-OES) was also reported by Florian et al. [65]. In contrast to all other samples, an additional peak at 457.3 eV in the Ti 2p spectra can be observed for *S2* with $F = 2.81$ J/cm^2 (Figure C1k) and $F = 4.76$ J/cm^2 (Figure C1h), characteristic for Ti^{3+} [62]. At the same time, the peak at 458.7 eV in Ti 2p reveals that Ti^{4+} concentration has decreased [59]. Interestingly additional peaks at 528.9 eV and 528.2 eV

appear in the O 1 s region of these samples, which might be assigned to metal sub oxides bound to unsaturated sites [66]. The deconvolution of the C 1 s spectra shows that carbon is implanted into the surface layer and can be attributed to the formation of metal (Ti and/or Al) carbides or oxicarbides with a binding energy of 283.2 eV [67]. At least in the case of Al, the formation of Al–C or Al–O–C is supported by the relative strong peak at 72.3 eV [67]. However, the formation of Ti^{3+} and of metal carbides at the sample surface is only observed for *S2* with $F = 2.81$ J/cm^2 and $F = 4.76$ J/cm^2. For scanning strategy *S2* a high *LO* of 90% is used so that each point on the sample is treated multiple times with each new line. Since laser-treated surfaces are highly reactive (e.g. oxidation) and show higher surface concentrations of adventitious carbon (compared to reference sample, see Table C1) [40] the high *LO* probably leads to incorporation of the adsorbed carbon species into the surface. Moreover, this could lead to a stabilization of lower oxidation states of the Ti when a structured and already oxidized/saturated spot is irradiated repeatedly with each new line. However, although the phenomenon of heat accumulation during LT cannot be directly inferred from the XPS data, different scanning strategies lead to the formation of various chemical groups in the near-surface layer, which is known to determine physical, biological, and chemical interactions. As already reported in literature, oxygen species affect the cell response on Ti [68]. Thus the relationship between oxide groups and other species generated at the surface and the cell behavior evoked with different scanning strategies should be considered for using materials after LT, for example, as implant material.

4. Conclusions

This study demonstrates morphological, crystallographic and chemical insights of self-organized nano- and microstructures on Ti6Al4V evoked by 300 fs-laser treatment. To the best of our knowledge, this is the first report describing the dynamic of the formation of self-organized structures with different scanning strategies with high repetition rates. The detailed investigations allow the following conclusions to be made:

(1) The formation of self-organized structures depends on the laser scanning strategy (level of pulse and line overlap) next to laser fluence.
(2) Small spatial distance between successive pulses with high repetition rates lead to the formation of melt due to pronounced heat accumulation during laser irradiation. Therefore, the growth mechanism of microstructures is dominated by heat-driven

phenomena (vapor–liquid solid growth and melt flow) depending on the fluence.

(3) A high scanning line overlap leads primarily to preferential valley ablation (PVA) next to VLS growth, depending on the fluence.

(4) Fs-laser treatment can lead to phase changes compared to originally present phases in received samples depending on fluence and the scanning strategy. Next to Ti-hcp and Ti-ccp, phases of Ti_6O, Ti_3Al were revealed by X-ray diffraction (XRD), which is in agreement with previous publications.

(5) Significant heat-affected-zones (HAZ) were observed after fs-laser treatment, which can extend several micrometers into the non-ablated material, especially at high fluences. This phenomenon has been given insufficient attention so far and should be considered when applying fs-treatment, since the HAZ is of critical relevance for the structural-mechanical performance of a component.

(6) Surface chemistry can be tailored by the scanning strategy and laser fluence. Ti have been observed by X-ray photoelectron spectroscopy (XPS) in oxidation states of $+ 2$, $+3$ and $+ 4$, respectively. These findings can, for instance, be used in future studies to evaluate biological interactions with laser-structured surfaces and the effects of various oxidation states on cell behavior.

Therefore, this study presents insights into the fundamental dynamics of the formation of self-organized structures. By investigation of different scanning strategies, the control of chemical, structural and morphological properties of self-organized structures is made possible and help to form guidelines for process designs to tailor large scale surfaces with preferred self-organized features.

The development of ultra-short pulsed laser systems with average powers of a few kW is progressing and will increasingly be used. Therefore, the findings of this study help to transfer stationary irradiation experiments to large areas and provide key information to use power scaling via high repetition rates. Beyond the scope of this study, mechanical and biological tests should be performed to evaluate the potential of surface properties and to research useful correlations with both scanning strategies. Further research should also investigate the influence of laser shock waves together with heat accumulation on the resulting phase composition after fs laser treatment. Via different settings for the applied repetition rate and fluence, the phase transformations need to be investigated in terms of critical laser settings for both phenomena and their contribution to temperature and deformation effects of the irradiated material.

CRediT authorship contribution statement

Georg Schnell: Conceptualization, Data curation, Investigation, Methodology, Visualization, Writing – original draft. **Henrik Lund:** Data curation, Investigation, Methodology, Visualization, Writing – original draft. **Stephan Bartling:** Data curation, Investigation, Methodology, Visualization, Writing – original draft. **Christian Polley:** Methodology, Writing – review & editing. **Abdullah Riaz:** Methodology, Writing – review & editing. **Volkmar Senz:** Investigation, Visualization. **Armin Springer:** Investigation, Visualization. **Hermann Seitz:** Resources, Supervision, Methodology, Writing – review & editing.

Declaration of Competing Interest

The authors declare that they have no known competing financial interests or personal relationships that could have appeared to influence the work reported in this paper.

Appendix A. Supplementary material

Supplementary data to this article can be found online at https://doi.org/10.1016/j.apsusc.2021.151115.

References

[1] G. Lütjering, J.C. Williams, Titanium: With 51 tables, 2. ed., Springer-Verlag, Berlin, Heidelberg, 2007.

[2] P.D. Miller, J.W. Holladay, Friction and wear properties of titanium, Wear 2 (2) (1958) 133–140, https://doi.org/10.1016/0043-1648(58)90428-9.

[3] H.W. Wiskott, U.C. Belser, Lack of integration of smooth titanium surfaces: a working hypothesis based on strains generated in the surrounding bone, Clin. Oral Implants Res. 10 (1999) 429–444, https://doi.org/10.1034/j.1600-0501.1999.100601.x.

[4] A. Cunha, A.P. Serro, V. Oliveira, A. Almeida, R. Vilar, M.-C. Durrieu, Wetting behaviour of femtosecond laser textured Ti–6Al–4V surfaces, Appl. Surf. Sci. 265 (2013) 688–696, https://doi.org/10.1016/j.apsusc.2012.11.085.

[5] G. Schnell, C. Jagow, A. Springer, M. Frank, H. Seitz, Time-Dependent Anisotropic Wetting Behavior of Deterministic Structures of Different Strut Widths on Ti6Al4V, Metals 9 (2019) 938, https://doi.org/10.3390/met9090938.

[6] C. Wang, H. Hu, Z. Li, Y. Shen, Y. Xu, G. Zhang, X. Zeng, J. Deng, S. Zhao, T. Ren, Y. Zhang, Enhanced Osseointegration of Titanium Alloy Implants with Laser Microgrooved Surfaces and Graphene Oxide Coating, ACS Appl. Mater. Interfaces 11 (43) (2019) 39470–39483, https://doi.org/10.1021/acsami.9b1273310.1021/acsami.9b12733.s001.

[7] Y.P. Kathuria, Laser microprocessing of metallic stent for medical therapy, J. Mater. Process. Technol. 170 (3) (2005) 545–550, https://doi.org/10.1016/j.jmatprotec.2005.05.041.

[8] E. Matthias, M. Reichling, J. Siegel, O.W. Kding, S. Petzoldt, H. Skurk, P. Bizenberger, E. Neske, The influence of thermal diffusion on laser ablation of metal films, Appl. Phys. A 58 (1994) 129–136, https://doi.org/10.1007/BF00332169.

[9] R. Le Harzic, N. Huot, E. Audouard, C. Jonin, P. Laporte, S. Valette, A. Fraczkiewicz, R. Fortunier, Comparison of heat-affected zones due to nanosecond and femtosecond laser pulses using transmission electronic microscopy, Appl. Phys. Lett. 80 (21) (2002) 3886–3888, https://doi.org/10.1063/1.1481195.

[10] S. Valette, E. Audouard, R. Le Harzic, N. Huot, P. Laporte, R. Fortunier, Heat affected zone in aluminum single crystals submitted to femtosecond laser irradiations. Applied Surface Science, 239(3-4), 381-386. Applied Surface Science 239 (2005) 381–386, doi:10.1016/J.APSUSC.2004.06.003.

[11] W. Pfleging, R. Kumari, H. Besser, T. Scharnweber, J.D. Majumdar, Laser surface textured titanium alloy (Ti–6Al–4V): Part 1 – Surface characterization, Appl. Surf. Sci. 355 (2015) 104–111, https://doi.org/10.1016/j.apsusc.2015.06.175.

[13] S. Valette, R. Le Harzic, N. Huot, E. Audouard, R. Fortunier, 2D calculations of the thermal effects due to femtosecond laser-metal interaction, Appl. Surf. Sci. 247 (1-4) (2005) 238–242, https://doi.org/10.1016/j.apsusc.2005.01.080.

[14] J. Bonse, J. Krüger, Probing the heat affected zone by chemical modifications in femtosecond pulse laser ablation of titanium nitride films in air. Journal of Applied Physics, 107(5), 054902. Journal of Applied Physics 107 (2010) 54902, doi: 10.1063/1.3311552.

[15] Y.R. Kolobov, E.V. Golosov, T.N. Vershinina, M.V. Zhidkov, A.A. Ionin, S. I. Kudryashov, S.V. Makarov, L.V. Seleznev, D.V. Sinitsyn, A.E. Ligachev, Structural transformation and residual stresses in surface layers of α + β titanium alloys nanotextured by femtosecond laser pulses, Appl. Phys. A 119 (2015) 241–247, https://doi.org/10.1007/s00339-014-8954-6.

[16] H. Thompson, J. Lammatao, M.D. Hecht, A. Yousif, B.R. Campbell, Y.N. Picard, Ultrashort Pulsed Laser Induced Heat Affected Zones Characterized by Ion Channeling Contrast Imaging, Microsc Microanal 20 (S3) (2014) 1480–1481, https://doi.org/10.1017/S1431927614009131.

[17] Y. Hirayama, M. Obara, Heat-affected zone and ablation rate of copper ablated with femtosecond laser, J. Appl. Phys. 97 (6) (2005) 064903, https://doi.org/10.1063/1.1852692.

[18] A.Y. Vorobyev, C. Guo, Direct femtosecond laser surface nano/microstructuring and its applications, Laser Photonics Rev. 7 (3) (2013) 385–407, https://doi.org/10.1002/lpor.201200017.

[19] E. Weingärtner, K. Wegener, C. Dold, in: CIRP Encyclopedia of Production Engineering, Springer Berlin Heidelberg, Berlin, Heidelberg, 2019, pp. 1006–1009, https://doi.org/10.1007/978-3-662-53120-4_6474.

[20] E. Stratakis, J. Bonse, J. Heitz, J. Siegel, G.D. Tsibidis, E. Skoulas, A. Papadopoulos, A. Mimidis, A.-C. Joel, P. Comanns, J. Krüger, C. Florian, Y. Fuentes-Edfuf, J. Solis, W. Baumgartner, Laser engineering of biomimetic surfaces, Materials Science and Engineering: R: Reports 141 (2020) 100562, https://doi.org/10.1016/j.mser.2020.100562.

[21] P.T. Mannion, J. Magee, E. Coyne, G.M. O'Connor, T.J. Glynn, The effect of damage accumulation behaviour on ablation thresholds and damage morphology in ultrafast laser micro-machining of common metals in air, Appl. Surf. Sci. 233 (1-4) (2004) 275–287, https://doi.org/10.1016/j.apsusc.2004.03.229.

[22] V. Oliveira, S. Ausset, R. Vilar, Surface micro/nanostructuring of titanium under stationary and non-stationary femtosecond laser irradiation, Appl. Surf. Sci. 255 (17) (2009) 7556–7560, https://doi.org/10.1016/j.apsusc.2009.04.027.

[23] S. Moradi, S. Kamal, P. Englezos, S.G. Hatzikiriakos, Femtosecond laser irradiation of metallic surfaces: effects of laser parameters on superhydrophobicity, Nanotechnology 24 (41) (2013) 415302, https://doi.org/10.1088/0957-4484/24/41/415302.

[24] J. Bonse, S. Gräf, Maxwell Meets Marangoni—A Review of Theories on Laser-Induced Periodic Surface Structures, Laser Photonics Rev. 14 (10) (2020) 2000215, https://doi.org/10.1002/lpor.v14.1010.1002/lpor.202000215.

[25] J. Bonse, S. Höhm, S. Kirner, A. Rosenfeld, J. Krüger, Laser-induced Periodic Surface Structures (LIPSS) – A Scientific Evergreen. In CLEO: QELS_Fundamental Science, Part of CLEO: 2016 : 5-10 June 2016, San Jose, California, United States. CLEO: Science and Innovations, San Jose, California; CLEO, Ed.; OSA, The Optical Society: Washington, D.C., USA, 2016; STh1Q.3, ISBN 978-1-943580-11-8.

[26] J. Bonse, S.V. Kirner, S. Höhm, N. Epperlein, D. Spaltmann, J. Krüger, Applications of laser-induced periodic surface structures (LIPSS). In Laser-based Micro- and Nanoprocessing XI. SPIE LASE, San Francisco, California, United States, Saturday 28 January 2017; Klotzbach, U., Washio, K., Kling, R., Eds.; SPIE, 2017; 100920N.

[27] J. Bonse, S. Kirner, M. Griepentrog, D. Spaltmann, J. Krüger, Femtosecond Laser Texturing of Surfaces for Tribological Applications, Materials (Basel) 11 (5) (2018) 801, https://doi.org/10.3390/ma11050801.

[28] C.A. Zuhlke, T.P. Anderson, D.R. Alexander, Formation of multiscale surface structures on nickel via above surface growth and below surface growth mechanisms using femtosecond laser pulses, Opt. Express 21 (7) (2013) 8460, https://doi.org/10.1364/OE.21.008460.

[29] E.J.Y. Ling, J. Saïd, N. Brodusch, R. Gauvin, P. Servio, A.-M. Kietzig, Investigating and understanding the effects of multiple femtosecond laser scans on the surface topography of stainless steel 304 and titanium, Appl. Surf. Sci. 353 (2015) 512–521, https://doi.org/10.1016/j.apsusc.2015.06.137.

[30] C. Florian Baron, A. Mimidis, D. Puerto, E. Skoulas, E. Stratakis, J. Solis, J. Siegel, Biomimetic surface structures in steel fabricated with femtosecond laser pulses: influence of laser rescanning on morphology and wettability, Beilstein J. Nanotechnol. 9 (2018) 2802–2812, https://doi.org/10.3762/bjnano.9.262.

[31] G. Schnell, U. Duenow, H. Seitz, Effect of Laser Pulse Overlap and Scanning Line Overlap on Femtosecond Laser-Structured Ti6Al4V Surfaces, Materials (Basel) 13 (4) (2020) 969, https://doi.org/10.3390/ma13040969.

[32] J.-T. Finger, Puls-zu-Puls-Wechselwirkungen beim Ultrakurzpuls-Laserabtrag mit hohen Repetitionsraten, 1. Auflage; Apprimus Verlag: Aachen, 2017, ISBN 9783863595418.

[33] R. Weber, T. Graf, P. Berger, V. Onuseit, M. Wiedenmann, C. Freitag, A. Feuer, Heat accumulation during pulsed laser materials processing, Opt. Express 22 (2014) 11312–11324, https://doi.org/10.1364/OE.22.011312.

[34] N.A. Inogamov, A.Y. Faenov, V.A. Khokhlov, V.V. Zhakhovskii, Y.V. Petrov, I. Y. Skobelev, K. Nishihara, Y. Kato, M. Tanaka, T.A. Pikuz, M. Kishimoto, M. Ishino, M. Nishikino, Y. Fukuda, S.V. Bulanov, T. Kawachi, S.I. Anisimov, V.E. Fortov, Spallative Ablation of Metals and Dielectrics, Contrib. Plasma Phys. 49 (7-8) (2009) 455–466, https://doi.org/10.1002/ctpp.v49:7/810.1002/ctpp.200910045.

[35] N.M. Bulgakova, I.M. Bourakov, Phase explosion under ultrashort pulsed laser ablation: modeling with analysis of metastable state of melt, Appl. Surf. Sci. 197–198 (2002) 41–44, https://doi.org/10.1016/S0169-4332(02)00300-8.

[36] S. Eaton, H. Zhang, P. Herman, F. Yoshino, L. Shah, J. Bovatsek, A. Arai, Heat accumulation effects in femtosecond laser-written waveguides with variable repetition rate, Opt. Express 13 (2005) 4708–4716, https://doi.org/10.1364/opex.13.004708.

[37] M. Sakakura, M. Shimizu, Y. Shimotsuma, K. Miura, K. Hirao, Temperature distribution and modification mechanism inside glass with heat accumulation during 250kHz irradiation of femtosecond laser pulses, Appl. Phys. Lett. 93 (23) (2008) 231112, https://doi.org/10.1063/1.3046101.

[38] F. Bauer, A. Michalowski, T. Kiedrowski, S. Nolte, Heat accumulation in ultra-short pulsed scanning laser ablation of metals, Opt. Express 23 (2015) 1035–1043, https://doi.org/10.1364/OE.23.001035.

[39] A.Y. Vorobyev, C. Guo, Femtosecond laser structuring of titanium implants, Appl. Surf. Sci. 253 (17) (2007) 7272–7280, https://doi.org/10.1016/j.apsusc.2007.03.006.

[40] G. Schnell, C. Polley, S. Bartling, H. Seitz, Effect of Chemical Solvents on the Wetting Behavior Over Time of Femtosecond Laser Structured Ti6Al4V Surfaces, Nanomaterials (Basel) 10 (2020), https://doi.org/10.3390/nano10061241.

[41] T.Y. Hwang, A.Y. Vorobyev, C. Guo, Ultrafast dynamics of femtosecond laser-induced nanostructure formation on metals. Applied Physics Letters, 95(12), 123111. Appl. Phys. Lett. 2009, 95, 123111, doi:10.1063/1.3222937.

[42] A.Y. Vorobyev, C. Guo, Femtosecond laser nanostructuring of metals, Opt. Express 14 (2006) 2164–2169, https://doi.org/10.1364/oe.14.002164.

[43] J. Bonse, A. Rosenfeld, J. Krüger, On the role of surface plasmon polaritons in the formation of laser-induced periodic surface structures upon irradiation of silicon by femtosecond-laser pulses, J. Appl. Phys. 106 (10) (2009) 104910, https://doi.org/10.1063/1.3261734.

[44] A.V. Zayats, I.I. Smolyaninov, Near-field photonics: surface plasmon polaritons and localized surface plasmons, J. Opt. A: Pure Appl. Opt. 5 (4) (2003) S16–S50.

[45] A.Y. Vorobyev, V.S. Makin, C. Guo, Periodic ordering of random surface nanostructures induced by femtosecond laser pulses on metals, J. Appl. Phys. 101 (3) (2007) 034903, https://doi.org/10.1063/1.2432288.

[47] S. He, J.J.J. Nivas, A. Vecchione, M. Hu, S. Amoruso, On the generation of grooves on crystalline silicon irradiated by femtosecond laser pulses, Opt. Express 24 (2016) 3238–3247, https://doi.org/10.1364/OE.24.003238.

[48] G.D. Tsibidis, C. Fotakis, E. Stratakis, From ripples to spikes: A hydrodynamical mechanism to interpret femtosecond laser-induced self-assembled structures, Phys. Rev. B 92 (2015) doi:10.1103/PhysRevB.92.041405.

[49] T.-Y. Derrien, T.E. Itina, R. Torres, T. Sarnet, M. Sentis, Possible surface plasmon polariton excitation under femtosecond laser irradiation of silicon, J. Appl. Phys. 114 (8) (2013) 083104, https://doi.org/10.1063/1.4818433.

[50] D.H. Lowndes, J.D. Fowlkes, A.J. Pedraza, Early stages of pulsed-laser growth of silicon microcolumns and microcones in air and SF6, Appl. Surf. Sci. 154–155 (2000) 647–658, https://doi.org/10.1016/S0169-4332(99)00369-4.

[51] G. Schnell, S. Staehlke, U. Duenow, J.B. Nebe, H. Seitz, Femtosecond Laser Nano/Micro Textured Ti6Al4V Surfaces-Effect on Wetting and MG-63 Cell Adhesion, Materials (Basel) 12 (13) (2019) 2210, https://doi.org/10.3390/ma12132210.

[53] F. Sánchez, J.L. Morenza, V. Trtik, Characterization of the progressive growth of columns by excimer laser irradiation of silicon, Appl. Phys. Lett. 75 (21) (1999) 3303–3305, https://doi.org/10.1063/1.125332.

[54] L. Lavisse, D. Grevey, C. Langlade, B. Vannes, The early stage of the laser-induced oxidation of titanium substrates, Appl. Surf. Sci. 186 (1-4) (2002) 150–155, https://doi.org/10.1016/S0169-4332(01)00761-9.

[55] Y.R. Kolobov, M.V. Zhidkov, E.V. Golosov, T.N. Vershinina, S.I. Kudryashov, S. V. Makarov, A.A. Ionin, A.E. Ligachev, Phase composition and structure of femtosecond laser-produced oxide layer on VT6 alloy surface, Laser Phys. Lett. 13 (7) (2016) 076103, https://doi.org/10.1088/1612-2011/13/7/076103.

[56] Z. Song, K. Nakata, A. Wu, J. Liao, Interfacial microstructure and mechanical property of Ti6Al4V/A6061 dissimilar joint by direct laser brazing without filler metal and groove, Mater. Sci. Eng., A 560 (2013) 111–120, https://doi.org/10.1016/j.msea.2012.09.044.

[57] A. Del Pérez Pino, P. Serra, J. Morenza, Oxidation of titanium through Nd:YAG laser irradiation, Appl. Surf. Sci. 197–198 (2002) 887–890, https://doi.org/10.1016/S0169-4332(02)00447-6.

[58] F.H. Chung, Quantitative interpretation of X-ray diffraction patterns of mixtures. I. Matrix-flushing method for quantitative multicomponent analysis, J Appl Crystallogr 7 (6) (1974) 519–525, https://doi.org/10.1107/S0021889874010375.

[59] E.C. Landis, K.C. Phillips, E. Mazur, C.M. Friend, Formation of nanostructured TiO 2 by femtosecond laser irradiation of titanium in O 2, J. Appl. Phys. 112 (6) (2012) 063108, https://doi.org/10.1063/1.4752276.

[60] J. Mildner, C. Sarpe, N. Götte, M. Wollenhaupt, T. Baumert, Emission signal enhancement of laser ablation of metals (aluminum and titanium) by time delayed femtosecond double pulses from femtoseconds to nanoseconds, Appl. Surf. Sci. 302 (2014) 291–298, https://doi.org/10.1016/j.apsusc.2013.09.137.

[62] M.C. Biesinger, L.W.M. Lau, A.R. Gerson, R.S.C. Smart, Resolving surface chemical states in XPS analysis of first row transition metals, oxides and hydroxides: Sc, Ti, V, Cu and Zn. *Applied Surface Science* 257 (3) (2010) 887–898, https://doi.org/10.1016/j.apsusc.2010.07.086.

[63] J.T. Kloprogge, L.V. Duong, B.J. Wood, R.L. Frost, XPS study of the major minerals in bauxite: gibbsite, bayerite and (pseudo-)boehmite, J. Colloid Interface Sci. 296 (2) (2006) 572–576, https://doi.org/10.1016/j.jcis.2005.09.054.

[65] C. Florian, R. Wonneberger, A. Undisz, S.V. Kirner, K. Wasmuth, D. Spaltmann, J. Krüger, J. Bonse, Chemical effects during the formation of various types of femtosecond laser-generated surface structures on titanium alloy, Appl. Phys. A 126 (2020) doi:10.1007/s00339-020-3434-7.

[66] P.M. Kumar, S. Badrinarayanan, M. Sastry, Nanocrystalline TiO2 studied by optical, FTIR and X-ray photoelectron spectroscopy: correlation to presence of surface states, Thin Solid Films 358 (1-2) (2000) 122–130, https://doi.org/10.1016/S0040-6090(99)00722-1.

[67] T.P. Nguyen, J. Ip, P. Jolinat, P. Destruel, XPS and sputtering study of the Alq3/electrode interfaces in organic light emitting diodes, Appl. Surf. Sci. 172 (1-2) (2001) 75–83, https://doi.org/10.1016/S0169-4332(00)00826-6.

[68] L.-H. Li, Y.-M. Kong, H.-W. Kim, Y.-W. Kim, H.-E. Kim, S.-J. Heo, J.-Y. Koak, Improved biological performance of Ti implants due to surface modification by micro-arc oxidation, Biomaterials 25 (14) (2004) 2867–2875, https://doi.org/10.1016/j.biomaterials.2003.09.048.